

A Finite Volume Method for Elastic Waves in Heterogeneous, Anisotropic and Fractured Media

Ingrid Kristine Jacobsen¹, Inga Berre¹, Jan Martin Nordbotten^{1,2}, Ivar Stefansson¹

¹ Center for Modeling of Coupled Subsurface, Dynamics, Department of Mathematics, University of Bergen, Allégaten 41, 5020 Bergen, Norway.

² NORCE Norwegian Research Centre AS

Abstract

Numerical modeling of elastic wave propagation in the subsurface requires applicability to heterogeneous, anisotropic and discontinuous media, as well as support of free surface boundary conditions. Here we study the cell-centered finite volume method Multi-Point Stress Approximation with weak symmetry (MPSA-W) for solving the elastic wave equation. Finite volume methods are geometrically flexible, locally conserving and they are suitable for handling material discontinuities and anisotropies. For discretization in time we have utilized the Newmark method, thereby developing an MPSA-Newmark discretization for the elastic wave equation. An important aspect of this work is the integration of absorbing boundary conditions into the MPSA-Newmark method to limit possible boundary reflections.

Verification of the MPSA-Newmark discretization is achieved through numerical convergence analyses in 3D relative to a known solution, demonstrating the expected convergence rates of order two in time and up to order two in space. With the inclusion of absorbing boundary conditions, the resulting discretization is verified by considering convergence in a quasi-1d setting, as well as through energy decay analyses for waves with various wave incidence angles. Lastly, the versatility of the MPSA-Newmark discretization is demonstrated through simulation examples of wave propagation in fractured, heterogeneous and transversely isotropic media.

Keywords: Finite volume method, elastic wave propagation, transversely isotropic media, absorbing boundary conditions, heterogeneous media.

1 Introduction

Modeling of elastic waves in the subsurface is important in understanding natural and induced earthquakes. Induced seismicity, e.g. related to geothermal energy extraction, CO₂-storage and wastewater disposal, takes place in locations characterized by complex material compositions. Specifically, heterogeneous and anisotropic rock formations with or without discontinuities such as fractures are highly relevant in all the abovementioned fields of application. Solving elastic wave propagation within such complex rock formations means that the numerical method must handle unstructured and general grids and material anisotropy and heterogeneity. Moreover, simulations involving the Earth's surface require employment of the free surface boundary condition.

Several numerical methods have been developed and utilized to solve the elastic wave propagation problem. Commonly studied methods within the research literature include those within the families of spectral element (SEM) and discontinuous Galerkin (dG) methods. Other methods such as finite difference (FD), pseudospectral (PSM), finite elements (FEM) and finite volume (FV) methods have also been studied. All these methods have their own advantages and drawbacks. For instance finite difference and spectral element methods are very efficient for elastic wave propagation problems, but they perform best in media without strong structural complexities (e.g. fractures) and material heterogeneities (Igel, 2016). On the other hand, finite volume and discontinuous Galerkin methods are naturally applicable to discontinuous and

heterogeneous media (Cardiff & Demirdžić, 2021; Keilegavlen & Nordbotten, 2017; Virieux et al., 2011), and they are flexible in terms of arbitrary cell shapes and unstructured grids (Cardiff & Demirdžić, 2021). For an overview of numerical methods for the elastic wave equation, we refer to Igel (2016) and Seriani and Oliveira (2020).

Finite volume and discontinuous Galerkin methods are closely related and share many advantageous properties. As already mentioned, they support general and unstructured grids which allow for representation of rather complex simulation domains. Such grid flexibility is crucial for accurately representing fractures and heterogeneous media where the material discontinuities do not coincide with orthogonal gridlines, as well as other geometrical complexities such as surface topography or boreholes (Igel, 2016). In addition to this, finite volume and discontinuous Galerkin methods can naturally enforce the free surface boundary condition, which is of high relevance in simulations including the Earth's surface. Although finite volume methods offer some advantageous properties, they are not among the most widely used for solving elastic wave propagation problems. This is due to finite volume methods often being restricted to lower order, while discontinuous Galerkin methods are easily extended to high order accuracy (Igel, 2016). However, the higher order accuracy comes at the expense of additional computational cost, which may not be appropriate when geometric features reduce the regularity of the solution.

As finite volume methods are widely used within the realm of flow in porous media, developing and utilizing finite volume methods for mechanical deformation makes it possible to have a unified solution approach for poroelastic solid-fluid interaction problems (Nordbotten, 2014). Common solution procedures for such coupled problems often include solving each of the subproblems with separate discretization schemes. See e.g. Kim et al. (2011) for an example of a finite element method for the mechanics and a finite volume method for the flow. Several works have focused on utilizing a finite volume method for both flow and mechanical deformation, providing a unified solution approach and consistent data structure for both subproblems (Nordbotten, 2016; Novikov et al., 2022; Terekhov, 2020; Terekhov & Vassilevski, 2022). All these works consider cell-centered finite volume methods for the coupled flow and static mechanical deformation problem. A natural extension is thus to develop finite volume methods for dynamic mechanical deformation/elastic wave propagation which can later, in a fully coupled manner, be used to solve poroelastic solid-fluid interaction problems with the inclusion of seismic effects.

There are several finite volume methods for mechanical deformation, and as we will highlight only a few, we refer to Cardiff and Demirdžić (2021) for an extensive review on finite volume methods for solid mechanics. The first application of a cell-centered finite volume method to solid mechanics was a method for homogeneous and isotropic linear elasticity by Demirdžić et al. (1988). Early developments of finite volume methods for elastic wave propagation include that of Dormy and Tarantola (1995) which use the velocity-displacement formulation of the elastic wave equation. Tadi (2004) proposed a second order accurate method for the second order displacement formulation with a focus on natural application of traction boundary conditions. Higher order finite volume methods for unstructured triangular and tetrahedral meshes include the arbitrary high order method by Dumbser et al. (2007). A more recent development is that of Zhang et al. (2016), which combines techniques of high order and spectral finite volume methods for the 2D problem. Zhang et al. (2017) presented an extension of this methodology to three spatial dimensions. Lemoine et al. (2013) used a high-resolution

finite volume method for wave propagation in orthotropic poroelastic media on cartesian grids, which was later expanded to nonrectilinear mapped grids by Lemoine and Ou (2014). Another finite volume method used for static mechanical deformation include the work of Tuković et al. (2013), which presents a detailed description of the finite volume discretization of multiple deformable bodies with different solid material parameters. Cell-centered finite volume methods for anisotropic and heterogeneous media include the multi-point stress approximation with weak symmetry (MPSA-W) by Keilegavlen and Nordbotten (2017), and the method of Terekhov and Tchelepi (2020).

The finite volume MPSA-W method, which is up to second order accurate, applies to general and unstructured grids, can naturally enforce the free surface boundary condition, and supports heterogeneous and anisotropic media. In addition to this, MPSA-W is the vector problem analogue of the finite volume Multi-Point Flux Approximation (MPFA) (Nordbotten & Keilegavlen, 2021; Aavatsmark, 2002), a spatial discretization that is shown to be a successful discretization method for solving problems within flow in porous media (Berre et al., 2021). MPSA-W is built on the same framework as MPFA, meaning the two methods hold the same advantages of computational efficiency due to minimal number of degrees of freedom and being able to solve problems in discontinuous, heterogeneous and anisotropic media. Thus, the MPFA and the MPSA-W are examples of two methods that can be combined for a seamlessly coupled solution procedure for poroelastic fluid-solid interaction problems. The MPFA-MPSA pair is available in simulation toolboxes such as the Porous Microstructure Analysis (PuMA) (Ferguson et al., 2018), the MATLAB Reservoir Simulation Toolbox (MRST) (Lie, 2019), as well as in PorePy (Keilegavlen et al., 2021) which is used herein.

Motivated by the properties of the MPSA-W method for (quasi)static elastic and poroelastic deformation problems in heterogeneous and anisotropic media, we present here for the first time a study of the MPSA-W method for solving the elastic wave propagation problem. The spatial discretization is applied in combination with a Newmark time integration scheme (Newmark, 1959), which is a second order accurate implicit time integration scheme widely used in computational solid mechanics. By combining the spatial discretization, MPSA-W, and the temporal discretization, Newmark, we obtain the MPSA-Newmark method. The MPSA-Newmark method is up to second order accurate in space and time, meaning it has balanced space/time accuracy for solving the elastic wave equation.

Solving the elastic wave equation poses the question of how to deal with possible wave reflections on the domain boundary. We have addressed this by employing the first order absorbing boundary conditions (ABCs) first presented by Clayton and Engquist (1977), which in practice are time dependent Robin-type boundary conditions. Therefore, this paper also provides a presentation of how time-dependent Robin boundary conditions are discretized in MPSA. As the structure of MPSA is like that of MPFA, the treatment of the boundary conditions is analogous in both discretization schemes. This analogy extends the applicability of the presented methodology for discretizing time-dependent Robin conditions to other multi-point finite volume schemes.

The structure of the paper is as follows. In Section 2, we present the mathematical model and the discretization. Section 3 presents verification of the code through convergence analyses and energy decay investigations. This is followed by simulations in anisotropic, heterogeneous and

fractured media in Section 4, which is highly relevant for the field of application, before concluding remarks are given in Section 5.

2 Methodology

This section covers the mathematical model and the discretization of the problem. We refer to Table 2.1 for an overview of the symbols used in the article.

Table 2.1: Nomenclature.

Symbol	Physical parameter	Unit
n, \mathbf{n}	Normal vector, discrete normal vector	—
\mathcal{C}	Stiffness tensor	$\text{kg m}^{-1}\text{s}^{-2}$
v	Symmetry axis vector for transversely isotropic media	—
\mathcal{R}	Robin weight	—
\mathcal{D}, \mathbf{D}	Robin weight for absorbing boundary conditions, discrete Robin weight for absorbing boundary conditions	$\text{kg m}^{-2}\text{s}^{-1}$
$\mathcal{D}_{\Delta t}, \mathbf{D}_{\Delta t}$	\mathcal{D} scaled with inverse of the time-step, discrete \mathbf{D} scaled with inverse of the time-step	$\text{kg m}^{-2}\text{s}^{-2}$
q, \mathbf{q}	Body force, discrete body force	$\text{kg m}^{-2}\text{s}^{-2}$
T, \mathbf{T}	Traction, discrete traction	$\text{kg m}^{-1}\text{s}^{-2}$
u, \mathbf{u}	Displacement, discrete displacement	m
$\dot{u}, \dot{\mathbf{u}}$	Velocity, discrete velocity	m s^{-1}
$\ddot{u}, \ddot{\mathbf{u}}$	Acceleration, discrete acceleration	m s^{-2}
σ	Stress tensor	$\text{kg m}^{-1}\text{s}^{-2}$
ϵ	Symmetric gradient of the displacement	m m^{-1}
τ	Internal traction weights	$\text{kg m}^{-2}\text{s}^{-2}$
w	Boundary traction weights	$\text{kg m}^{-2}\text{s}^{-2}$
ρ	Density	kg m^{-3}
λ	First Lamé parameter	$\text{kg m}^{-1}\text{s}^{-2}$
λ_{\parallel}	Transverse compressive stress parameter	$\text{kg m}^{-1}\text{s}^{-2}$
λ_{\perp}	Perpendicular compressive stress parameter	$\text{kg m}^{-1}\text{s}^{-2}$
μ	Second Lamé parameter/Shear modulus	$\text{kg m}^{-1}\text{s}^{-2}$
μ_{\parallel}	Transverse shear parameter	$\text{kg m}^{-1}\text{s}^{-2}$
μ_{\perp}	Transverse-to-perpendicular shear parameter	$\text{kg m}^{-1}\text{s}^{-2}$
c_p	Primary wave speed	m s^{-1}
θ	Wave rotation angle	rad
\mathcal{E}_u	Relative discrete L^2 -error of displacement	—
\mathcal{E}_T	Relative discrete L^2 -error of traction	—
E	Energy	J
E_0	Initial energy	J
Ω	Simulation domain	m^2 or m^3
ω	Anisotropic region in Ω	m^2 or m^3
t	Time	s
β	Time-discretization parameter	—
γ	Time-discretization parameter	—
Δt	Time-step size	s
n (as superscript)	Time-step number	—

$$\frac{\Delta x}{\nabla} \quad \left| \begin{array}{l} \text{Grid size} \\ \text{Nabla-operator} \end{array} \right. \quad \left| \begin{array}{l} \text{m} \\ \text{m}^{-1} \end{array} \right.$$

2.1 Governing Equations

2.1.1 The Elastic Wave Equation

We consider propagation of elastic waves in a three-dimensional domain denoted Ω , the reduction to two spatial dimensions being straightforward. As our interest is in elastic waves, we will only consider infinitesimal deformations in an elastic material. The equation for conservation of momentum then takes the form:

$$\rho \ddot{u} = \nabla \cdot \sigma + q \quad \text{in } \Omega. \quad (2.1)$$

Here ρ is the rock density, $u = [u_x, u_y, u_z]^T$ is the displacement, σ is the stress tensor, q is an external body force and, using the dot notation for derivatives in time, \ddot{u} is the acceleration. The constitutive stress-strain relationship is given for small deformations by Hooke's law as:

$$\sigma = \mathcal{C} : \epsilon(u), \quad (2.2)$$

where \mathcal{C} is the fourth order stiffness tensor and $\epsilon(u)$ is the symmetric gradient of u :

$$\epsilon(u) = \frac{1}{2} (\nabla u + (\nabla u)^T). \quad (2.3)$$

For future reference, we present two examples of the stiffness tensor \mathcal{C} . First, we present \mathcal{C} for an isotropic medium:

$$\mathcal{C}_{ijkl} = \lambda \delta_{ij} \delta_{kl} + \mu (\delta_{ik} \delta_{jl} + \delta_{il} \delta_{jk}), \quad (2.4)$$

where λ is the first Lamé parameter, μ is the second Lamé parameter, or the shear modulus, and δ_{ij} is the Kronecker delta, taking the value 1 if $i = j$, and 0 otherwise. Secondly, we will present \mathcal{C} for a transversely isotropic medium (Payton, 2012). Transversely isotropic media are represented by five independent material parameters, as opposed to only two as is the case for the isotropic stiffness tensor. The stiffness tensor for transversely isotropic media, where the axis of symmetry aligns with the unit vector $v = (v_1, v_2, v_3)^T$, is as follows:

$$\begin{aligned} \mathcal{C}_{ijkl} = & (\lambda + \lambda_{||}) \delta_{ij} \delta_{kl} + \mu_{||} (\delta_{ik} \delta_{jl} + \delta_{il} \delta_{jk}) - \lambda_{||} (\delta_{ij} v_k v_l + \delta_{kl} v_i v_j) \\ & + (\mu_{\perp} - \mu_{||}) (\delta_{ik} v_j v_l + \delta_{jk} v_i v_l + \delta_{il} v_j v_k + \delta_{jl} v_i v_k) \\ & + (\lambda_{||} + \lambda_{\perp} + 2\mu_{||} - 2\mu_{\perp}) v_i v_j v_k v_l, \quad \text{for } i, j, k, l = 1, 2, 3. \end{aligned} \quad (2.5)$$

Here λ is the first Lamé parameter, $\lambda_{||}$ and λ_{\perp} are the transverse and perpendicular compressive stress parameters, respectively, and $\mu_{||}$ and μ_{\perp} are the transverse and transverse-to-perpendicular shear parameters, respectively. Notice that by setting $\lambda_{||} = \lambda_{\perp} = 0$ and $\mu_{||} = \mu_{\perp}$, the dependence on v is eliminated from Equation (2.5). In that case, Equation (2.5) reduces to Equation (2.4), that is, the stiffness tensor for an isotropic solid.

To close the mathematical model, we have initial and boundary conditions. The boundary conditions are detailed in dedicated sections below, while the initial conditions are included in Section 2.2.3.

2.1.2 Boundary conditions

We denote the boundary of the domain as Γ , which we subdivide into four non-overlapping parts, $\Gamma = \Gamma_N \cup \Gamma_D \cup \Gamma_R \cup \Gamma_A$. These are identified as the Neumann, Dirichlet, Robin and Absorbing boundaries, respectively. We summarize these below.

Neumann boundary conditions are specified in terms of prescribed tractions, F_N :

$$\sigma \cdot n = F_N \quad \text{on } \Gamma_N, \quad (2.6a)$$

where n is the outward pointing normal vector relative to the boundary. Dirichlet boundary conditions are specified in terms of prescribed displacements, F_D :

$$u = F_D \quad \text{on } \Gamma_D. \quad (2.6b)$$

Robin conditions are specified as a weighted sum of traction and displacement at the boundary, with prescribed data F_R having units of traction:

$$\sigma \cdot n + \mathcal{R}u = F_R \quad \text{on } \Gamma_R. \quad (2.6c)$$

The coefficient \mathcal{R} is a 2-tensor weight for the displacement component of the Robin conditions.

It is often desirable to eliminate wave reflections at the boundaries when solving the elastic wave equation. A natural choice is to employ boundary conditions that effectively allow outward-going waves to pass through without reflection, often referred to as absorbing boundary conditions. We consider here one of the simplest forms of absorbing boundary conditions, namely the first order ones by Clayton and Engquist (1977) which absorb waves at normal incidence exactly (Higdon, 1991). There will be some reflection for other incidence angles, but nevertheless a reduction compared to that of Dirichlet or Neumann conditions. The absorbing conditions by Clayton and Engquist were originally expressed with displacements and displacement gradients, but were later expressed in terms of displacements and tractions by Tsogka (1999). We utilize the latter formulation

$$\sigma \cdot n + \mathcal{D}\dot{u} = F_A \quad \text{on } \Gamma_A, \quad (2.7)$$

where $\mathcal{D} = \left(\sqrt{\rho(\lambda + 2\mu)} nn^T + \sqrt{\rho\mu}(I - nn^T) \right)$. The time dependent component of the boundary condition is the time derivative of the boundary displacement, namely the velocity, \dot{u} . For the sake of generality, we have included a non-zero forcing term F_A , with the understanding that the absorbing boundary condition is recovered by setting $F_A = 0$.

When referring to the boundary data in general, we will sometimes simply refer to F , understanding that the subscript should be clear from context.

2.2 Discretization

In this section we will summarize the main structure of the space-time discretization, emphasizing the novel aspects of this work.

2.2.1 Multi-Point Stress Approximations Including Boundary Conditions

To simplify the exposition, we restrict the presentation to polyhedral domains Ω . We then consider a non-overlapping set \mathcal{T} of k cells $K_i \in \mathcal{T}$ for $i = 1, 2, \dots, k$, such that $\bigcup_{K_i \in \mathcal{T}} \overline{K_i} = \Omega$. A face on the boundary of a cell is denoted by f and is collected in the set of all faces, \mathcal{F} . The set of faces for a particular cell K , is denoted \mathcal{F}_K . In a similar manner, neighboring cells of a face, f , are denoted \mathcal{T}_f . Figure 2.1 provides an illustration of an internal face f_1 (red) and the corresponding \mathcal{T}_{f_1} (marked in pink). Cells, K , have volumes, m_K , and faces f have measures m_f . Boundary related grid quantities follow the same notation as mentioned above, but with a tilde. For instance, \tilde{f} represents a boundary face, and the set of all boundary faces is $\tilde{\mathcal{F}} \subset \mathcal{F}$. The set of boundary faces sharing a vertex with a face f is denoted $\tilde{\mathcal{F}}_f$. We refer to Figure 2.1 for an illustration of the face f_2 (blue) which touches the boundary and the corresponding $\tilde{\mathcal{F}}_{f_2}$ (marked in black). Finally, sets of Dirichlet, Neumann, Robin or Absorbing boundary faces will have subscripts D , N , R or A , analogously to their continuous counterparts. Figure 2.1 illustrates a two-dimensional unstructured grid with the grid-related quantities we will use to present MPSA and boundary conditions, but the same relations hold also in three spatial dimensions.

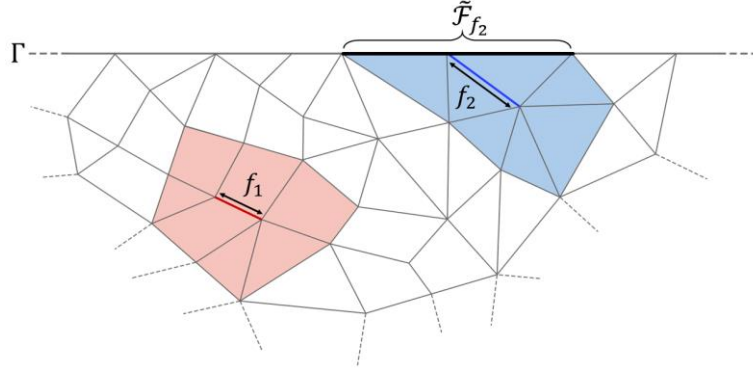


Figure 2.1: Illustration of grid related quantities used to express the Multi-Point Stress Approximation and the discrete boundary conditions. The pink shaded area is the stencil for approximating the flux over the internal face f_1 marked in red. The blue shaded area and the boundary faces, $\tilde{\mathcal{F}}_{f_2}$, marked in black, represent the stencil for approximating the flux over the face f_2 marked in blue that has an edge touching the boundary, Γ .

Integrating Equation (2.1) over a cell, $K \in \mathcal{T}$, and applying the divergence theorem gives

$$\int_K (\rho \ddot{u} - q) dV = \int_{\partial K} \sigma \cdot n_{\partial K} dA, \quad (2.8)$$

where $n_{\partial K}$ is the outward pointing normal vector of the boundary, ∂K , of cell K .

Dividing the surface integral into two sums of face tractions leads to the following general expression which holds for any finite volume method:

$$\int_{\partial K} \sigma \cdot n_{\partial K} dA = \sum_{f \in \mathcal{F}_K \setminus \tilde{\mathcal{F}}_{K,N}} \int_f \sigma \cdot n_{K,f} dA + \sum_{\tilde{f} \in \tilde{\mathcal{F}}_{K,N}} \int_{\tilde{f}} \sigma \cdot n_{K,\tilde{f}} dA. \quad (2.9)$$

Here we have separated the sum into faces that lie on a Neumann boundary (where the traction is known directly from the boundary conditions) and remaining faces. We now define cell-averaged displacements and face-averaged tractions as:

$$\mathbf{u}_K = \frac{1}{m_K} \int_K \mathbf{u} \, dV \quad \text{and} \quad \mathbf{T}_{K,f} = \frac{1}{m_f} \int_f \boldsymbol{\sigma} \cdot \mathbf{n}_{K,f} \, dA.$$

Here the bold font indicates that \mathbf{u} and \mathbf{T} are finite-dimensional vectors. Moreover, we note that since for any two cells K and K' sharing a face f , the definition of the face traction only differs by the orientation of $\mathbf{n}_{K,f}$. Therefore, due to the continuity of traction, it is clear that $\mathbf{T}_{K,f} = -\mathbf{T}_{K',f}$. Defining analogously the cell-averaged source term, and considering that density is piece-wise constant, Equation (2.8) becomes the space-discrete (but still continuous in time) system of ordinary differential equations:

$$m_K(\rho \ddot{\mathbf{u}}_K - \mathbf{q}_K) = \sum_{f \in \mathcal{F}_K \setminus \tilde{\mathcal{F}}_{K,N}} m_f \mathbf{T}_{K,f} + \sum_{\tilde{f} \in \tilde{\mathcal{F}}_{K,N}} m_{\tilde{f}} \mathbf{F}_{\tilde{f}}, \quad (2.10)$$

where $\ddot{\mathbf{u}}_K$ and \mathbf{q}_K are, respectively, the discrete acceleration and source for cell K , and $\mathbf{F}_{\tilde{f}}$ is the face-averaged Neumann boundary data for face $\tilde{f} \subset \Gamma_N$.

Equation (2.10) represents conservation of energy on each finite volume K , and holds for all (spatial) finite volume approximations to the elastic wave equations. What distinguishes the various methods is how Hooke's law is approximated, in the sense of expressing $\mathbf{T}_{K,f}$ in terms of cell displacements \mathbf{u} . Most finite volume methods for elasticity, including the MPSA methods, are designed to be both linear as well as "local", the latter in the sense that in the interior of the domain the approximation of $\mathbf{T}_{K,f}$ only depends on the set $\mathcal{T}_f \subset \mathcal{T}$ of cells that share a vertex with the face f (see the pink shaded region in Figure 2.1). For faces touching the boundary, like the face colored in blue in Figure 2.1, the approximation of $\mathbf{T}_{K,f}$ will include the set $\tilde{\mathcal{F}}_f \subset \mathcal{F} \cap \Gamma$ of boundary faces sharing a vertex with f . This set is clearly empty for faces strictly in the interior of the domain. We limit the exposition to this class of methods, which implies that each traction can be written as:

$$\mathbf{T}_{K,f} = \sum_{L \in \mathcal{T}_f} \tau_{K,f,L} \mathbf{u}_L + \sum_{g \in \tilde{\mathcal{F}}_f} w_{K,f,g} \mathbf{F}_g. \quad (2.11)$$

The precise definition of the internal weights $\tau_{K,f,L}$ is not essential to the current presentation, and we refer to Keilegavlen and Nordbotten (2017) for details. We emphasize that the definition of the boundary weights $w_{K,f,g}$ depend on the type of boundary. Again, the previously mentioned reference is sufficient for defining the coefficients associated with the time-independent boundary conditions (i.e. Neumann, Dirichlet, and Robin). However, that work did not consider absorbing boundary conditions, and we will detail the inclusion of such boundary conditions below.

The finite volume methods considered herein do not deal with the time-dependent aspect of boundary conditions, as they are exclusively defined as spatial discretizations. Therefore, the time derivative in Equation (2.7) must be discretized in time. Anticipating that we will use a second order accurate implicit scheme to discretize the acceleration term, we choose to consider a two-step implicit second order scheme for the boundary conditions, providing enhanced accuracy over a first-order method. This provides the following time-discrete representation of the absorbing boundary conditions:

$$\sigma^n \cdot n + \mathcal{D}_{\Delta t} u^n = \mathcal{D}_{\Delta t} \left(\frac{4}{3} u^{n-1} - \frac{1}{3} u^{n-2} \right) + F_A, \quad (2.12)$$

where $\mathcal{D}_{\Delta t} = \frac{3}{2\Delta t} \mathcal{D}$ and Δt denotes the time-step size. The symbol n is used for both the normal vector and the time-step number, where the distinction lies in whether n is a superscript. When used in a superscript, n denotes the time-step number. Quantities with superscript $(n - k)$ correspond to the quantity at k time-steps back in time.

We recognize that the implicit problem to be solved, Equation (2.12), is on the form of a Robin boundary condition (see Equation (2.6c)) where the Robin weight $\mathcal{D}_{\Delta t}$ scales as the inverse of the time-step. As such, we note that the implementation of the absorbing boundary conditions is from a spatial perspective equivalent to implementing Robin boundary conditions with a non-zero data term obtained from the previous two time-steps. The fully discrete equation for the tractions on non-Neumann boundaries is thus:

$$\begin{aligned} \mathbf{T}_{K,f}^n = & \sum_{L \in \mathcal{J}_f} \tau_{K,f,L} \mathbf{u}_L^n + \sum_{g \in \tilde{\mathcal{F}}_f \cap (\Gamma \setminus \Gamma_A)} w_{K,f,g} \mathbf{F}_g^n \\ & + \sum_{g \in \tilde{\mathcal{F}}_f \cap \Gamma_A} w_{K,f,g} \left(\mathcal{D}_{\Delta t} \left(\frac{4}{3} \mathbf{u}_g^{n-1} - \frac{1}{3} \mathbf{u}_g^{n-2} \right) + \mathbf{F}_g^n \right) \end{aligned} \quad (2.13)$$

We emphasize that the coefficients $w_{K,f,g}$ for the absorbing boundary conditions are calculated as for Robin boundaries with Robin weights $\mathcal{D}_{\Delta t}$.

2.2.2 The Newmark Method

For discretization in time on the internal part of the domain we use the second order accurate Newmark method, which is widely used for solid mechanics. The original formulation of the Newmark method reads (Newmark, 1959):

$$\dot{u}^n = \dot{u}^{n-1} + (1 - \gamma) \Delta t \ddot{u}^{n-1} + \gamma \Delta t \ddot{u}^n, \quad (2.14)$$

$$u^n = u^{n-1} + \Delta t \dot{u}^{n-1} + \frac{\Delta t^2}{2} [(1 - 2\beta) \ddot{u}^{n-1} + 2\beta \ddot{u}^n], \quad (2.15)$$

where β and γ are the Newmark discretization parameters.

The primary variable of the MPSA discretization is displacement, meaning that we solve the linear system with the displacements as the unknowns. The Newmark method can be adapted to suit the formulation of displacements as the only unknowns by rearranging Equations (2.14) and (2.15) (Chopra, 2012). This provides us with the following expressions for the current time-step velocity and acceleration:

$$\dot{u}^n = \left(1 - \frac{\gamma}{\beta} \right) \dot{u}^{n-1} + \Delta t \left[1 - \gamma - \frac{\gamma(1 - 2\beta)}{2\beta} \right] \ddot{u}^{n-1} + \frac{\gamma}{\beta \Delta t} (u^n - u^{n-1}), \quad (2.16)$$

$$\ddot{u}^n = \frac{1}{\beta \Delta t^2} \left[u^n - u^{n-1} - \Delta t \dot{u}^{n-1} - (1 - 2\beta) \frac{\Delta t^2}{2} \ddot{u}^{n-1} \right]. \quad (2.17)$$

2.2.3 The Fully Discretized Model

The fully discretized model is obtained by combining the spatial and temporal discretizations presented in Sections 2.2.1 and 2.2.2. Substituting the discrete numerical tractions (Equation (2.13)) and the Newmark acceleration (Equation (2.17)) into the space-discrete system of ordinary differential equations represented by Equation (2.10) provides the fully discrete elastic wave equation and boundary conditions with displacements as the unknowns. To close the system of discretized equations, we assign initial boundary displacement values for the two previous time-steps (see Equation (2.13)), and initial values of displacement, velocity and acceleration on the internal part of the domain on the previous time-step. After initialization, the fully discretized model equations are solved for the displacements. After the displacements are obtained, the velocity and acceleration are updated according to Equations (2.16) and (2.17), respectively.

3 Convergence Analysis

This section presents convergence analysis of the MPSA-Newmark method with different types of boundary conditions. The first subsection is dedicated to convergence analysis of the MPSA-Newmark method with Dirichlet boundary conditions, where the analysis includes both a theoretical and a numerical part. The second subsection contains numerical convergence analysis of the MPSA-Newmark method with absorbing boundary conditions.

We now define the following L^2 -norms for the cell quantity \mathbf{u} and the face quantity \mathbf{T} :

$$\|\mathbf{u}\|_{\mathcal{T}} = \left(\sum_{K \in \mathcal{T}} m_K \mathbf{u}_K^2 \right)^{\frac{1}{2}}, \quad (3.1)$$

$$\|\mathbf{T}\|_{\mathcal{F}} = \left(\sum_{f \in \mathcal{F}} \frac{1}{D} m_f (d_L - d_R) \cdot n_f \mathbf{T}_f^2 \right)^{\frac{1}{2}}, \quad (3.2)$$

where $L, R \in \mathcal{T}_f$ in such a way that $\mathcal{F}_L \cap \mathcal{F}_R \neq \emptyset$. The symbol d_L denotes the vector pointing from the face-center, x_f , of f to the cell-center, x_L , of L . Similarly, d_R is the vector pointing from x_f to x_R . The symbol n_f denotes the face normal vector pointing from cell R to cell L , and the symbol D represents the dimension of the simulation domain. In the case of $f \in \tilde{\mathcal{F}}$, one of d_L, d_R is the zero vector.

The numerical errors of cell- and face-centered quantities are computed relative to the exact solutions projected onto cell-centers and face-centers. Hence, we introduce the projection $\Pi_{\mathcal{T}}$ which returns a cell-centered quantity $((\Pi_{\mathcal{T}}\mathbf{u})_K = u(x_K))$ and the projection $\Pi_{\mathcal{F}}$ which returns a face-centered quantity $((\Pi_{\mathcal{F}}\mathbf{T})_f = T(x_f))$. Then, considering plain type symbols to denote exact analytical solutions and boldface symbols to denote discrete solutions, the relative L^2 -errors, \mathcal{E} , are computed according to:

$$\mathcal{E}_u = \frac{\|\mathbf{u} - \Pi_{\mathcal{T}}\mathbf{u}\|_{\mathcal{T}}}{\|\Pi_{\mathcal{T}}\mathbf{u}\|_{\mathcal{T}}}, \quad (3.3)$$

$$\mathcal{E}_T = \frac{\|\mathbf{T} - \Pi_{\mathcal{F}}T\|_{\mathcal{F}}}{\|\Pi_{\mathcal{F}}T\|_{\mathcal{F}}}. \quad (3.4)$$

Subscript u and T on the error symbol denote displacement and traction errors, respectively. All errors are computed at the final time.

Runscripts for generating all the numerical results presented in the following sections are accessible in the Docker image found in Jacobsen et al. (2024).

3.1 Convergence of MPSA-Newmark with Dirichlet Boundary Conditions

The combination of MPSA and Newmark can be understood in the context of the so-called ‘‘Method of Lines’’ (MoL). Thus, we consider the problem after spatial discretization as a semi-discrete problem (discrete in space and continuous in time), to which we thereafter apply the temporal discretization to resolve the time evolution. This perspective is advantageous, as the MoL is known to converge to the full solution of the time-space problem under quite weak conditions for the spatial and temporal discretization (see e.g. Knabner and Angermann (2003), Verwer and Sanz-Serna (1984)). Relevant for the current study is that for the space-time discretization to be convergent, the temporal discretization needs to be C-stable (see Definition 4.1 in (Verwer & Sanz-Serna, 1984)) independent of the stiffness of the problem arising from the spatial discretization (Verwer & Sanz-Serna, 1984). A common choice for stable discretization of second-order derivatives in time is the Newmark method, and in particular with the parameter choices $\beta = 1/4$ and $\gamma = 1/2$. This parameter choice provides a stable and energy conserving scheme (see e.g. (Subbaraj & Dokainish, 1989)), and is also the choice we employ in the current work. Due to the linearity of our model problem, the convergence rate will be limited by the convergence rate of the spatial and temporal discretization schemes. In particular, let ψ denote convergence rate of the temporal method. The spatial convergence of the primary variable, namely the displacement u , is denoted by ϕ_u , while that of the secondary variable, namely the traction, T , is denoted by ϕ_T . We then expect the space-time approximation, where all errors are computed at the final time, to satisfy:

$$\begin{aligned} \|\mathbf{u} - \Pi_{\mathcal{T}}\mathbf{u}\|_{\mathcal{T}} &= \mathcal{O}((\Delta x)^{\phi_u} + (\Delta t)^{\psi}), \\ \|\mathbf{T} - \Pi_{\mathcal{F}}\mathbf{T}\|_{\mathcal{F}} &= \mathcal{O}((\Delta x)^{\phi_T} + (\Delta t)^{\psi}), \end{aligned} \quad (3.5)$$

where Δx denotes the grid size. For the MPSA method, the convergence rates are established numerically to be $\phi_u = 2$ and $1 < \phi_T \leq 2$ for a broad class of grids (Keilegavlen & Nordbotten, 2017; Nordbotten & Keilegavlen, 2021). For the Newmark method with the abovementioned parameter choice, the convergence rate is $\psi = 2$ (Subbaraj & Dokainish, 1989). The temporal convergence rate of $\psi = 2$ is expected hold for both displacements and tractions. We note that the spatial traction error will dominate in the case of refining with equal rates in both space and time, resulting in a lower convergence of the tractions than that of the displacements in a combined space-time convergence analysis.

Numerical convergence analysis of the MPSA-Newmark with Dirichlet boundary conditions is performed with a known analytical solution in two and three dimensions for both Cartesian and simplex grids. We performed the analysis on a unit square domain in 2D and a unit cube

domain in 3D, and all material parameters hold unitary values corresponding to an isotropic solid. The body force term, q , in Equation (2.1) as well as initial values for displacement, velocity and acceleration are chosen in accordance with the analytical solutions (see Appendix A for the expressions). The analytical solution holds zero Dirichlet boundary conditions. For the sake of brevity, only the results of the combined space and time 3D convergence analyses on simplex grids are presented. The analytical solution of the displacement for the convergence analysis is $u = [u_x, u_y, u_z]^T$, where each component of the solution u is determined by:

$$u_i = \sin\left(\frac{5\pi}{2}t\right)xyz(1-x)(1-y)(1-z), \quad i \in x, y, z. \quad (3.6)$$

An illustration of the discrete solution at the final time ($t = 1.0$ s) is presented in Figure 3.1.

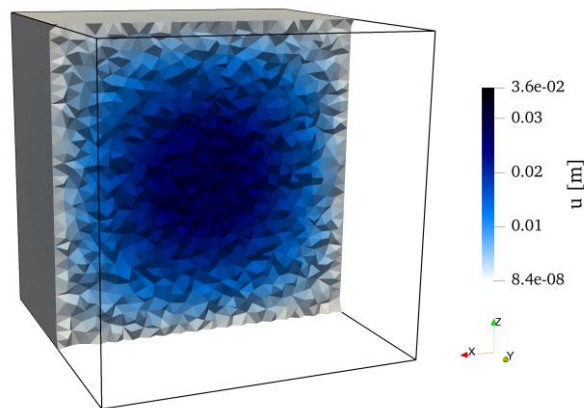


Figure 3.1: Illustration of what the displacement profile looks like at time $t=1.0$ s for the finest convergence analysis grid.

The results from the convergence analysis are displayed in Table 3.1 and Figure 3.2. We see that the displacement error converges with 2nd order while the traction error converges with between 1st and 2nd order, which are the expected rates.

Table 3.1: Combined space time convergence error table.

Refinement	Number of cells	Time-step size [s]	Displacement error	Traction error
Initial	387	1.0/150	3.32e-01	3.46e-01
First	2570	1.0/300	5.88e-02	7.44e-02
Second	19071	1.0/600	1.45e-02	2.24e-02
Third (final)	148129	1.0/1200	3.60e-03	7.86e-03

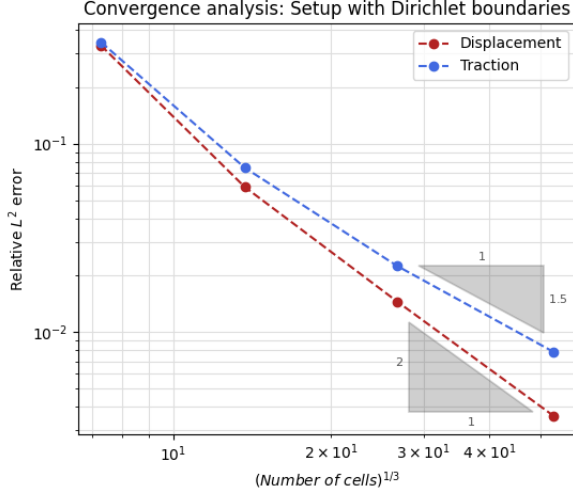


Figure 3.2: Error plot for the combined spatial and temporal convergence analysis of MPSA-Newmark with Dirichlet boundaries.

We also performed analyses in space and time separately. These analyses provided a convergence rate of 2 for displacements and between 1 and 2 for tractions in space, and a convergence rate of 2 for both displacements and tractions in time. The related error values and convergence plot are omitted from the text for the sake of brevity. Runscripts which reproduce the error values for the separate time and space convergence analyses are provided in the Docker image found in Jacobsen et al. (2024).

3.2 Convergence of MPSA-Newmark with Absorbing Boundary Conditions

The absorbing boundary conditions introduce a first-order derivative in time which we discretize by a second-order implicit method. Thus, the temporal discretization of the problem becomes a combination of Newmark and the second-order implicit method. Therefore, the convergence rates for Dirichlet boundary conditions cannot necessarily be expected to carry over to a model with absorbing boundary conditions. In this section we therefore present numerical convergence analyses of the MPSA-Newmark scheme for the setup with absorbing boundary conditions. Parameters that are common for all the simulations in this section are shown in Table 3.2.

Table 3.2: Simulation parameters for orthogonal and diagonal waves.

Symbol	Value	Unit
λ	0.01	$\text{kg m}^{-1} \text{s}^{-2}$
μ	0.01	$\text{kg m}^{-1} \text{s}^{-2}$
t_{final}	15.0	s
Ω	$[0, 1.0]^2$	m

3.2.1 Orthogonal Waves

The absorbing boundary conditions are investigated in a quasi-1D setting to demonstrate their effectiveness. The setup is quasi-1D in the sense that it is run in a 2D unit square, but all off-diagonal components of the stiffness tensor are removed. As we are only interested in a wave that propagates parallel to the x -axis, values of the displacement, velocity and acceleration in directions other than the x -direction are zero. The analytical solution for the displacement, $u(x, t)$ is thus the following:

$$u(x, t) = \left[\sin\left(t - \frac{x}{c_p}\right), 0 \right]^T. \quad (3.7)$$

Here c_p is the primary wave speed ($c_p = \sqrt{\frac{\lambda+2\mu}{\rho}}$). The simulation is initiated with values for the displacement, and the corresponding velocity and acceleration.

The wave is maintained by a time dependent Dirichlet condition on the left boundary after initialization. The right boundary is absorbing and is expected to perfectly absorb waves at normal incidence. We have zero Neumann conditions on the top and bottom boundaries. See Figure 3.3 for a schematic of the domain and its boundary conditions.

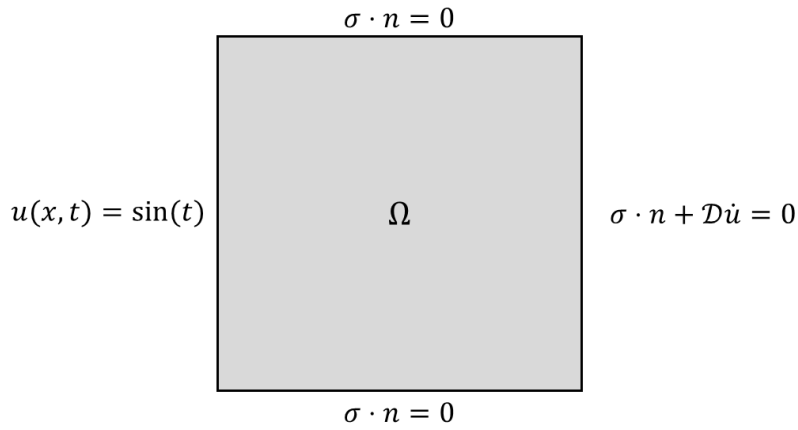


Figure 3.3: Schematic of domain boundary conditions for the quasi-1D test setup.

A plot of the relative L^2 -errors computed at the final time with successive refinement in both space and time is shown in Figure 3.4 (see Table 3.3 for mesh and time-step values). We observe second order convergence for both displacements and tractions, which are the optimal rates for the scheme.

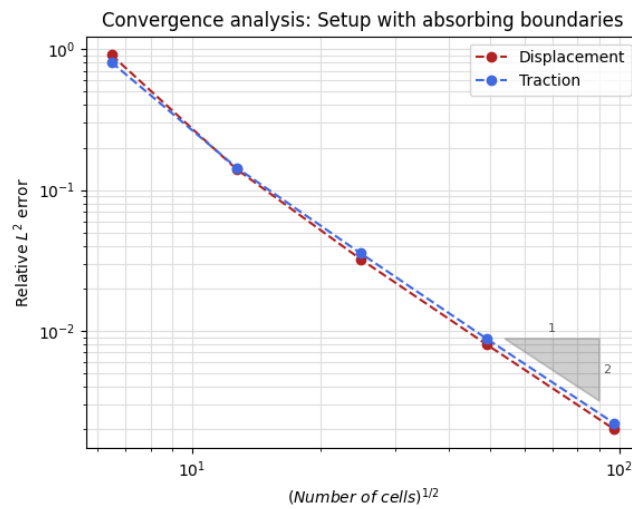


Figure 3.4: Convergence plot for the combined temporal and spatial analysis of MPSA-Newmark with absorbing boundaries.

Table 3.3: Time-step values and cell numbers for the temporal and spatial convergence analysis of MPSA-Newmark with absorbing boundary conditions.

	Value	Unit
Initial number of cells	42	—
Number of cells, first refinement	162	—
Number of cells, second refinement	616	—
Number of cells, third refinement	2400	—
Final number of cells	9520	—
Initial Δt	1.0	s
Δt , first refinement	0.5	s
Δt , second refinement	0.25	s
Δt , third refinement	0.125	s
Final Δt	0.0625	s

3.2.2 Diagonal Waves

In this problem setup we investigate how well the absorbing boundary conditions absorb non-orthogonal waves. The domain now has absorbing boundary conditions on all boundary sides, and the wave is being imposed by initial values for displacement, velocity and acceleration.

The absorbing boundary conditions are only perfectly absorbing for waves at normal incidence angles, but they are expected to have an effect on other incidence angles as well. Therefore, as there are no driving forces present in the system, the system energy is expected to decrease towards zero as time passes. The system energy is described by $E = \sum_{K \in \mathcal{T}} \int_K \rho \dot{\mathbf{u}}_K^2 dV$, where $\dot{\mathbf{u}}_K$ is the numerical velocity in cell K .

The expression for the initial displacement wave is as follows:

$$u(x, y, t = 0) = \begin{bmatrix} \cos(\theta) \sin\left(-\frac{\cos(\theta)x + \sin(\theta)y}{c_p}\right) \\ \sin(\theta) \sin\left(-\frac{\cos(\theta)x + \sin(\theta)y}{c_p}\right) \end{bmatrix}. \quad (3.8)$$

Derivation of the initial displacement, as well as the expressions for the initial velocity and acceleration, are presented in Appendix B. We refer to Figure 3.5 for an illustration of the initial displacement profile for both an orthogonal wave and a rotation of the orthogonal wave.

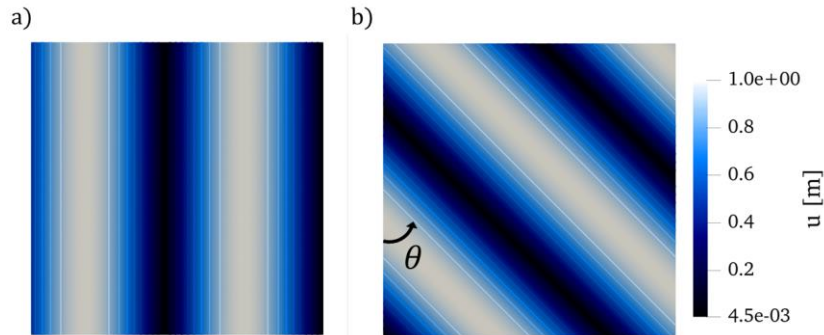


Figure 3.5: Displacement magnitude profile with contour lines for a) an orthogonal wave. b) a rotation of the orthogonal wave.

In Figure 3.6 we show the temporal evolution of the ratio between the energy, E , and the initial energy, E_0 . The energy decay analysis is performed for various grid sizes where all the domains contain a wave rotated by $\frac{\pi}{4}$ rad. The right dashed line in Figure 3.6 corresponds to when a $\frac{\pi}{4}$ rad-rotated wave has exited the domain, while the left dashed line corresponds to when an orthogonal wave has exited domain. The region between the two dashed lines is thus the time interval where waves rotated at angles between 0 and $\frac{\pi}{4}$ rad have exited the domain. The simulation is run until a final time of $t = 15.0$ s with a time-step $\Delta t = 1/20$ s. Grid sizes and the corresponding number of cells are listed in Table 3.4.

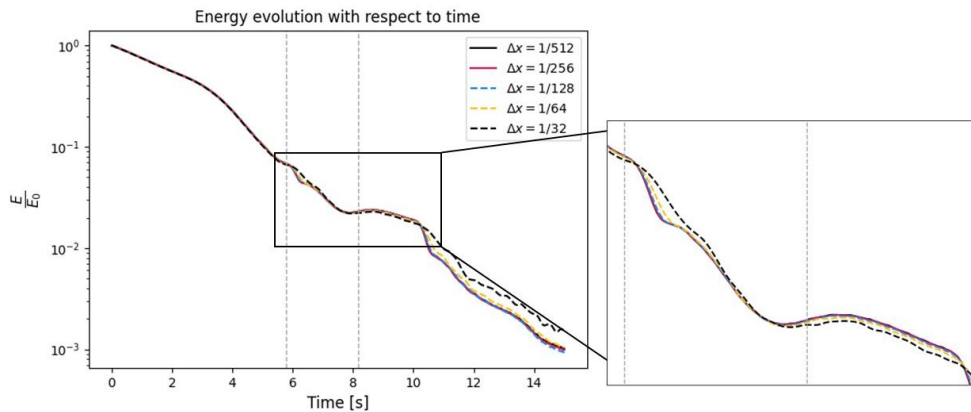


Figure 3.6: Energy evolution as time passes for different grid sizes, Δx . The wave rotation angle is held constant at $\pi/4$. The figure shows the system energy for the entire simulation time.

Table 3.4: Grid sizes and corresponding number of cells for the energy decay analysis with successive grid refinement.

	Grid size, Δx [m]	Number of cells
Initial refinement	1/32	2400
First refinement	1/64	9520
Second refinement	1/128	37976
Third refinement	1/256	151724
Final refinement	1/512	606 496

In Figure 3.6 we see that the energy decay can be divided into three phases: Decreasing, then plateauing and finally decreasing again. These three phases can be explained by the emergence of a spurious low-velocity wave as the simulation starts running. Looking to Figure 3.7 a) we see a wave which propagates towards the upper right corner of the domain once the time-stepping starts. As it propagates, since no new wave is introduced to the domain, there is a discontinuity in the solution along the bottom and left lateral boundary. This causes the emergence of a spurious wave in the lower left corner, which is common when using higher order time discretization schemes in the presence of discontinuities (see Figure 3.7 a) and b)). Referring to Figure 3.7 c), which is a snapshot from after the initialized wave has exited the domain, we can see that the spurious wave is still present due to its significantly lower propagation speed. The energy of this wave is represented by the energy plateau between 8.0 s and 10.0 s in Figure 3.6. When the slow wave finally exits the domain after around 10.0 seconds, we see a rapid decrease in the system energy.

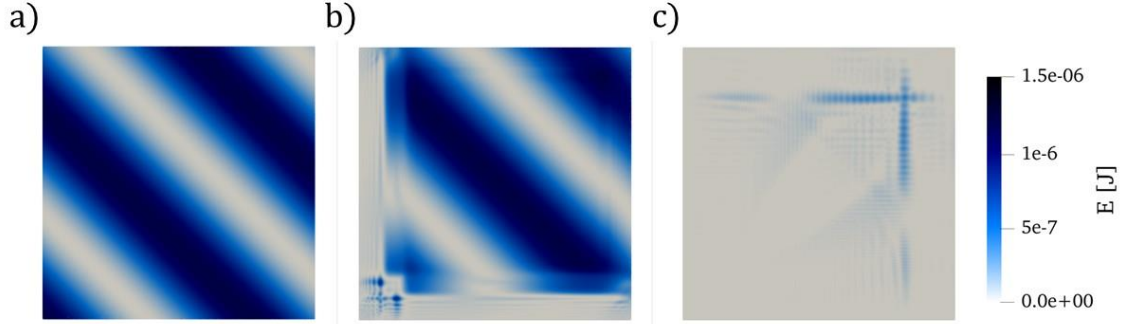


Figure 3.7: Discrete energy distribution in a domain with 606496 cells. a) At initialization ($t = 0.0$ s), b) At $t = 1.0$ s. c) At $t = 8.5$ s, which is when the initial wave has exited and only the initialization artifact remains.

To further investigate the performance of the absorbing boundary conditions, we considered waves rotated with different values of the rotation angle, θ . The energy decay results are presented in Figure 3.8. Values for the time-step size and cell number for the simulations with different rotation angles correspond to the final and finest refinement values that are presented in Table 3.3.

We see in Figure 3.8 that the system energy decreases for all the values of θ that we tested. We also see that the simulation whose wave rotation angle is $\theta = 0$ has the highest remaining energy after $t = 15.0$ s. Note that the setup with $\theta = 0$ in the present section and the quasi-1D setup presented in Section 3.2.1 are not the same: In the quasi-1D setup, all shear components of the stiffness tensor were removed. Additionally, the top and bottom boundary were stress free. The waves in the quasi-1D setup were thus allowed to propagate undisturbed along the top and bottom boundaries. The setup with $\theta = 0$ in the present section has absorbing boundaries on all the domain boundaries and the shear components of the stiffness tensor are not removed. In practice this means that the waves are travelling parallel to a boundary which only absorbs waves at a normal incidence angle perfectly. Absorption of waves travelling in a direction parallel to the boundary is less effective, which explains a higher remaining energy in that case.

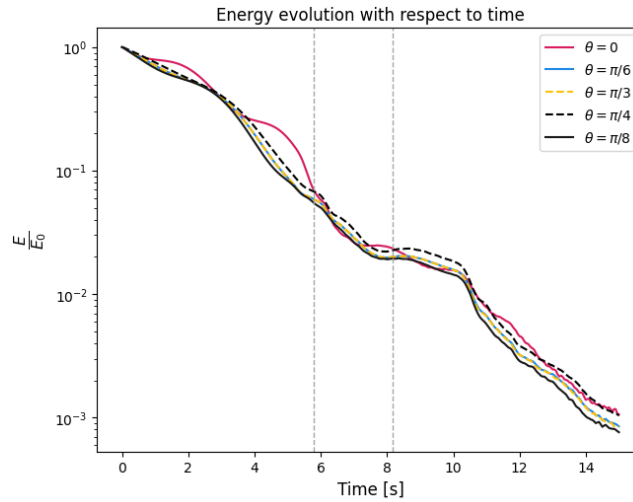


Figure 3.8: Energy evolution as time passes for different rotation angles, θ .

4 Wave Propagation in Anisotropic and Heterogeneous Media

4.1 Example 1: Simulations with Different Seismic Source Locations

In this section we present wave propagation in anisotropic and heterogeneous media where the simulation domain, Ω , is a unit cube. The domain is heterogeneous in the sense that it contains both isotropic and anisotropic regions. The anisotropic region is located fully inside Ω and is denoted by ω . We consider the anisotropic domain to be transversely isotropic with the z-axis as the axis of symmetry. The stiffness tensor for the anisotropic region is determined by five independent material parameters as presented in Equation (2.5), while the isotropic part of the domain has a stiffness tensor according to Equation (2.4).

The dimensions and location of the anisotropic region are specified for each simulation example. We refer to Figure 4.1 for an illustration of an example domain where the anisotropic region is located at the domain center and has side lengths of 0.5 m. Parameters for the simulation examples are listed in Table 4.1.

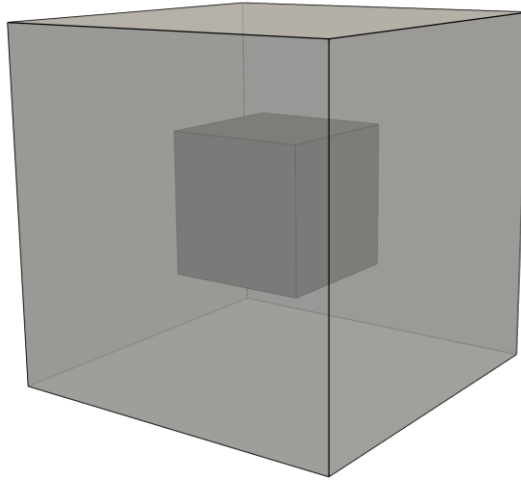


Figure 4.1: Illustration of a 3D cubic domain with an inner domain. The lighter part of the domain is isotropic, while the darker, inner part is transversely isotropic. The location of the inner domain differs for the different simulation examples.

Waves are introduced to the domain by a Ricker wavelet, which is commonly employed for modeling seismic sources. The simulation is initialized by zero initial displacement, zero initial acceleration and a velocity determined by the expression

$$\dot{u}(x, y, z) = e^{-\frac{\pi^2((x-x_R)^2+(y-y_R)^2+(z-z_R)^2)}{0.125^2}} [x - x_R, y - y_R, z - z_R]^T. \quad (4.1)$$

The velocity in Equation (4.1) corresponds to a Ricker wavelet, where $(\cdot)_R$ are the coordinate values for the center of the wavelet. The coordinate values are specified for each simulation example.

The dimensions of the outer and inner domain, as well as the material parameters for each of the domains, are held the same for both the simulation examples. The only difference between the two simulations is the location of the internal domain and the location of the wave source. An overview of the simulation parameters for the simulation examples is presented in Table 4.1.

Table 4.1 Simulation parameters for the heterogeneous and anisotropic simulations

	Symbol	Value	Unit
Common parameters	Ω	$[0, 1.0]^3$	m^3
	# cells	512 000	–
	Δt	1/600	s
	t_{final}	0.15	s
Isotropic domain parameters	μ	1.0	$\text{kg m}^{-1} \text{s}^{-2}$
	λ	1.0	$\text{kg m}^{-1} \text{s}^{-2}$
Anisotropic domain parameters	$\mu_{ }$	1.0	$\text{kg m}^{-1} \text{s}^{-2}$
	μ_{\perp}	2.0	$\text{kg m}^{-1} \text{s}^{-2}$
	$\lambda_{ }, \lambda_{\perp}$	5.0	$\text{kg m}^{-1} \text{s}^{-2}$
	λ	1.0	$\text{kg m}^{-1} \text{s}^{-2}$
Location parameters for source within inner domain (Ex. 1.1)	ω	$[0.25, 0.75]^3$	m^3
	(x_R, y_R, z_R)	(0.5, 0.5, 0.5)	(m, m, m)
Location parameters for source within outer domain (Ex. 1.2)	ω	$[0.25, 0.75] \times [0.25, 0.75] \times [0.05, 0.55]$	m^3
	(x_R, y_R, z_R)	(0.5, 0.5, 0.7)	(m, m, m)

4.1.1 Example 1.1: Ricker source located within the anisotropic domain

We expect different wave propagation behaviors in isotropic and anisotropic domains. In isotropic materials we expect the waves to propagate uniformly in all directions, just like an expanding sphere. In anisotropic media the waves are expected to deviate from the radial symmetry that occurs in isotropic media, meaning that the wave can for instance have an ellipsoidal shape instead of a spherical one.

Using a transversely isotropic medium for the domain should allow us to observe both expected behaviors described above. The transversely isotropic medium considered herein has the z-axis as the axis of symmetry, meaning that the xy -plane is the plane of isotropy. The waves are thus expected to behave in an isotropic manner in the xy -plane, while all other planes are expected to hold distorted wave patterns.

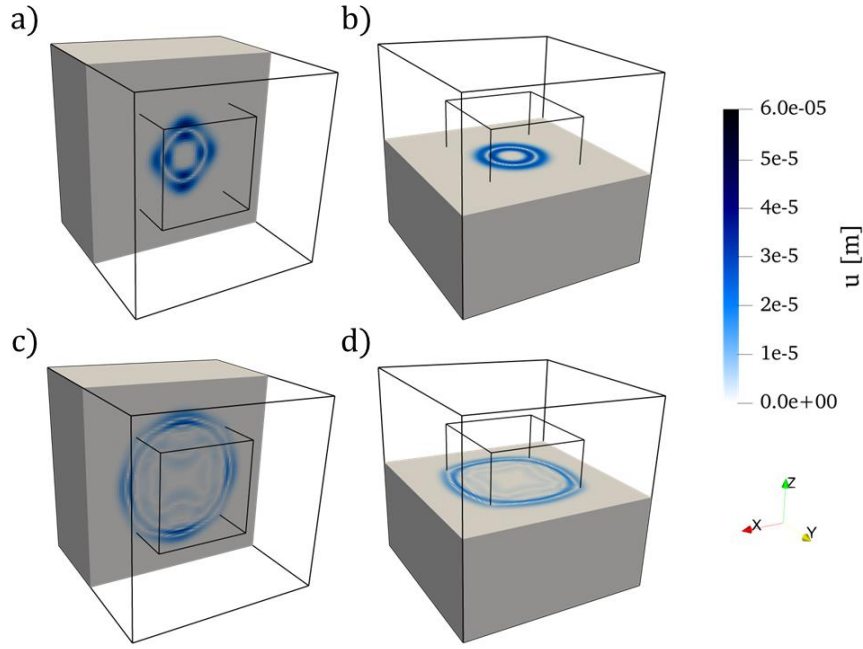


Figure 4.2: Wave propagation where the wave is imposed inside the anisotropic domain. The first row contains snapshots from time $t = 0.05$ s. The second row contains snapshots from time $t = 0.125$ s.

Looking to Figure 4.2 a)-d) we see the wave propagation at two different times and in two different planes. The black outline within Ω represents the anisotropic region, ω . Figure 4.2 b) illustrates a radial symmetry of the displacement wave, which is as expected as the figure depicts the displacement profile in the xy -plane (plane of isotropy) at a point in time where the wave has not yet exited the anisotropic region. On the other hand, Figure 4.2 a) and c) show only axial symmetry due to the anisotropies in the domain, while subfigure d) shows axial symmetry because the displacement wave now has propagated into the isotropic region. Additionally, subfigures c) and d) show that some reflections occur at the internal material discontinuity boundaries.

4.1.2 Example 1.2: Ricker source located outside the anisotropic domain

We will demonstrate elastic wave propagation in heterogeneous media further by locating the wave source outside the anisotropic region. As we saw in Section 4.1.1, there are wave reflections caused by intersections of material layers with different properties. When a wave travels towards and through heterogeneities, we also expect that both the shape and the propagation speed of the wave are altered. Depending on the values of the material parameters, the wave can move either faster or slower. In the case of the simulation presented in this section, we expect a higher propagation speed through the anisotropic domain due to higher values of λ , λ_{\perp} , μ_{\parallel} and μ_{\perp} (see Table 4.1).

As the Ricker wavelet is allowed to propagate through the isotropic medium, it eventually hits the anisotropic region, ω , which is indicated by the black outline within Ω . In Figure 4.3 we see that the circular shape of the Ricker wavelet becomes distorted within the anisotropic region. Specifically, the wave travels quicker through the anisotropic region, just as expected from the choice of material parameters. In addition to this we see in Figure 4.3 c) and d) that a wave is reflected at the internal boundary.

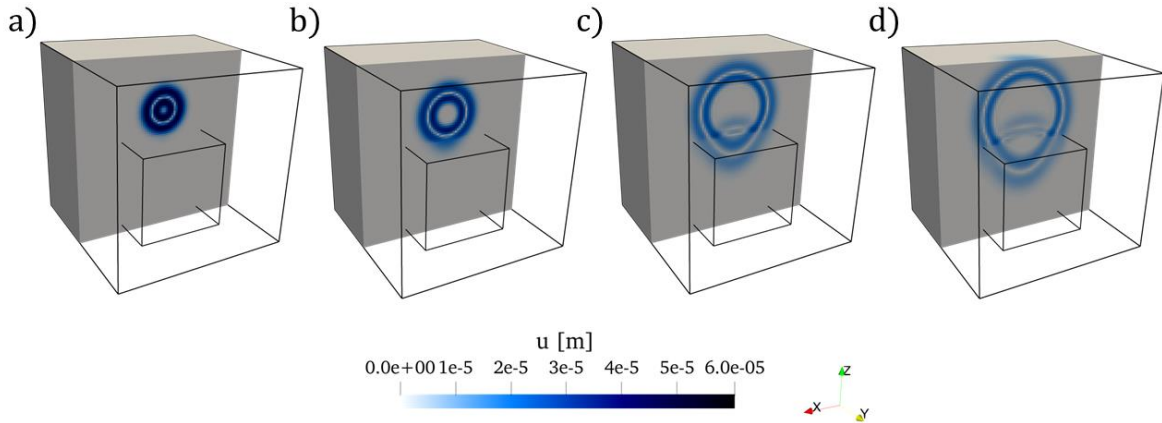


Figure 4.3: Propagation of Ricker wavelet and encounter with an internal domain boundary. Time a) $t = 0.05$ s, b) $t = 0.075$ s, c) $t = 0.125$ s, d) $t = 0.15$ s.

4.2 Example 2: Simulation in Heterogeneous and Fractured Media

As outlined in the introduction, we are interested in applications related to the subsurface where the rock formations may be heterogeneous and fractured. Therefore, we present this example as a demonstration that we can use the present methodology, namely the MPSA-Newmark with absorbing boundary conditions, to investigate problems in such media.

The domain is divided into three isotropic layers with different material parameters. Parameters for the upper, middle and lower layer are presented in Table 4.2. We enforce absorbing boundary conditions on all the outer domain boundaries, and inside the domain we have an internal Neumann boundary with zero traction ($\sigma \cdot n = 0$) which models an open fracture. The open fracture, which is a rectangular plane with corners in the points $(0.2, 0.2, 0.8)$, $(0.2, 0.8, 0.8)$, $(0.8, 0.8, 0.2)$ and $(0.8, 0.2, 0.2)$, is indicated in blue in the schematic of the domain in Figure 4.4.

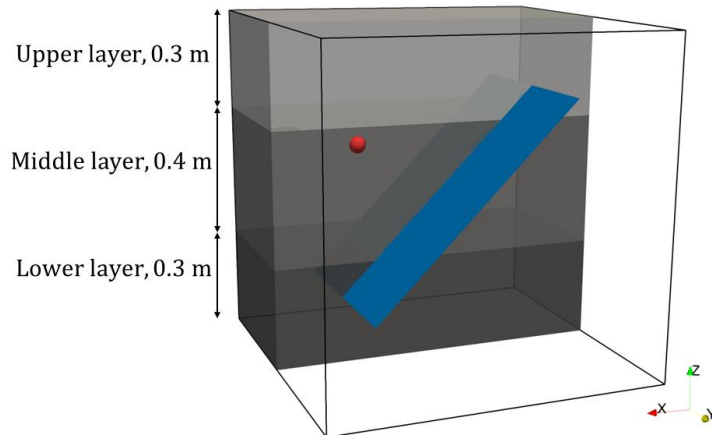


Figure 4.4: Schematic of fractured and layered heterogeneous medium used in example 2. The red sphere indicates where the seismic source is located and the blue plane represents an open fracture. The domain is cut at $y = 0.5$ m such that we get a cross-section view of the inside of the medium. Partial transparency is applied to show the fracture plane within the rock matrix.

Like in Section 4.1 we stimulate the domain by a Ricker wavelet. That is, zero initial displacement and acceleration, and a velocity corresponding to the Ricker wavelet expression shown below.

$$\dot{u}(x, y, z) = e^{-\frac{\pi^2((x-0.75)^2+(y-0.5)^2+(z-0.65)^2)}{0.3^2}}[x - 0.75, y - 0.5, z - 0.65]^T. \quad (4.2)$$

This corresponds to a Ricker wavelet centered at the point $(x, y, z) = (0.75, 0.5, 0.65)$. The location of the Ricker wavelet center is indicated by a red sphere in Figure 4.4.

We expect the wave to be reflected when it hits the fracture. No displacement waves should cross the open fracture, and we thus expect to see a sudden drop in displacement magnitude just beyond where the fracture is located. As the medium consists of layers of different parameter values, we also expect some reflections from the internal layer boundaries as well as different wave propagation speeds in the different layers, like that in Figure 4.3.

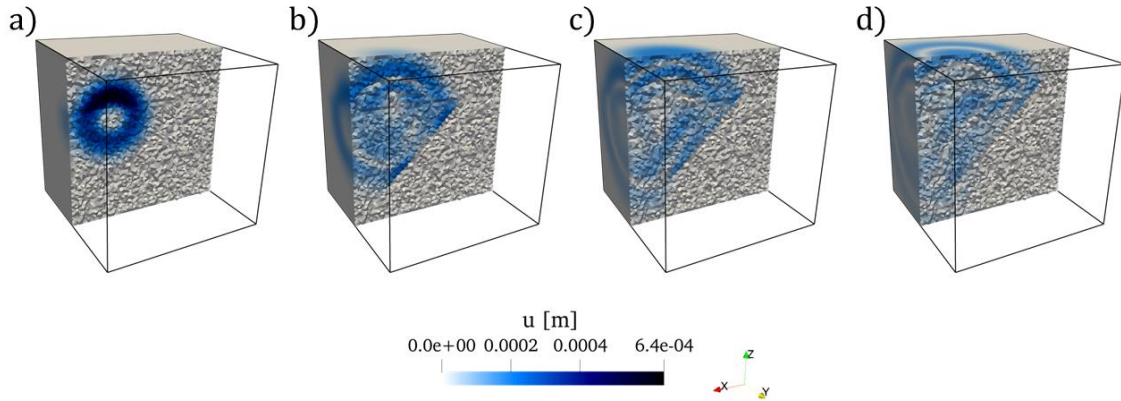


Figure 4.5: Wave propagation in layered heterogeneous and fractured medium at four different time-steps: a) $t = 0.05$ s, b) $t = 0.125$ s, c) $t = 0.175$ s, d) $t = 0.225$ s.

Figure 4.5 illustrates how the wave propagates in the heterogeneous and fractured domain. Specifically, the figure shows that the wave is reflected as it hits the open fracture. Additionally, the outer domain boundaries allow for the wave to propagate outwards, leaving no visible artificial boundary reflections. Figure 4.5 also shows, especially in the yz -plane, wider waves in the lower layer. This is expected from the higher material parameters in this region than those found in the two other domain layers.

To illustrate the sudden drop in displacement magnitude across the fracture, we have plotted the displacement along the diagonal black line that is shown in Figure 4.6 a). The displacement along the line is presented in Figure 4.6 b), and it is shown that the displacement magnitude suddenly drops to zero at a distance of $1/\sqrt{2}$ m along the diagonal line. This is where the fracture is located, and the displacement drop indicates that the wave is fully reflected by the fracture.

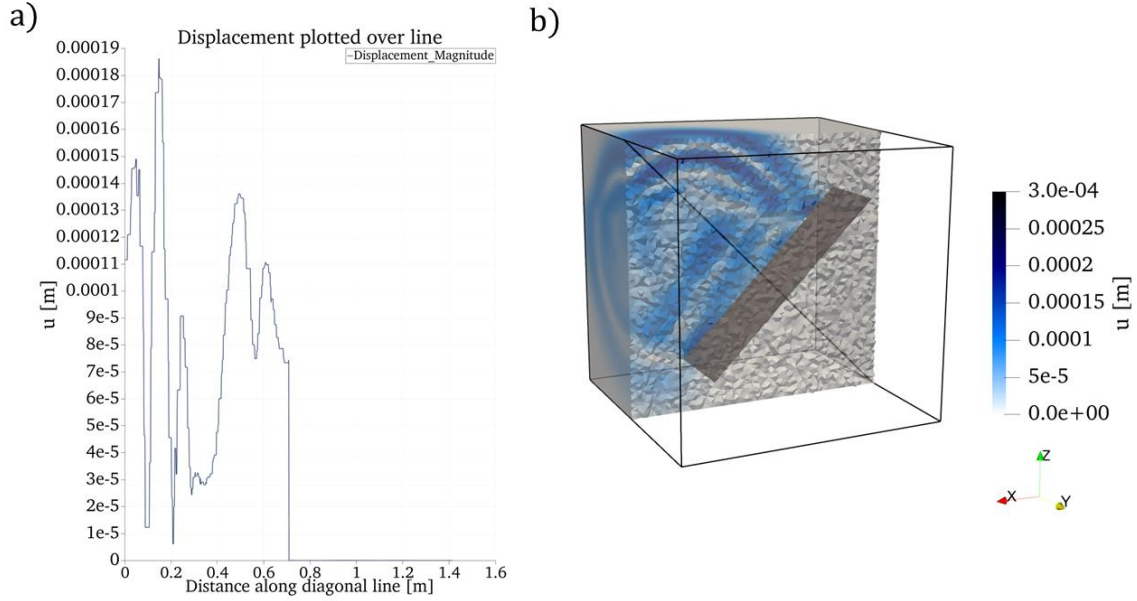


Figure 4.6: Demonstration of the wave being reflected of the fracture at time $t = 0.1875$ s. a) The displacement magnitude along the black diagonal line shown in subfigure b). b) Simulation domain cut at $y = 0.5$ m to visualize the wave propagation inside the domain. Partial transparency of the domain is applied to better visualize the dark grey fracture plane and the black diagonal line.

Table 4.2: Simulation parameters for example 2.

	Symbol	Value	Unit
Upper layer	λ	1.0	$\text{kg m}^{-1} \text{s}^{-2}$
	μ	1.0	$\text{kg m}^{-1} \text{s}^{-2}$
Middle layer	λ	2.0	$\text{kg m}^{-1} \text{s}^{-2}$
	μ	2.0	$\text{kg m}^{-1} \text{s}^{-2}$
Lower layer	λ	3.0	$\text{kg m}^{-1} \text{s}^{-2}$
	μ	3.0	$\text{kg m}^{-1} \text{s}^{-2}$
Other parameters	(x_R, y_R, z_R)	(0.75, 0.5, 0.65)	(m, m, m)
	Ω	$[0, 1.0]^3$	m^3
	t_{final}	0.25	s
	Δt	$5.0 \cdot 10^{-4}$	s
	# cells	877 945	—

5 Conclusions

We have presented the MPSA-Newmark method with absorbing boundary conditions for the elastic wave equation. The presentation includes verification and analysis of the MPSA-Newmark method, as well as a demonstration of the method's capabilities in two and three spatial dimensions. Convergence analyses of the MPSA-Newmark method were first performed and presented for the case with Dirichlet conditions. The convergence analysis provided the expected rates of up to 2 in space and a rate of 2 in time.

For the case with absorbing boundaries the convergence analysis shows that the solution converges with second order in both time and space. We also studied how effective the

absorbing boundaries were for waves coming in at an angle different from normal incidence. We observe that the system energy decays for all incidence angles tested, indicating that the boundary conditions absorb a significant amount of the energy in the system. Grid refinement analysis for a wave rotated by an angle of $\frac{\pi}{4}$ rad showed the same qualitative behavior of the energy decay for all grid sizes tested, where the finest grid resulted in the lowest final energy. The presence of residual energy is expected due to the wave's non-orthogonal incidence angle.

Finally, a demonstration of the method's capabilities when it comes to discontinuities, heterogeneity and anisotropy was shown. We first presented two simulation examples highlighting anisotropic and heterogeneous effects. An example where the seismic source is in the anisotropic part of the domain demonstrates how the code reproduces that waves behave in an isotropic way in the plane of isotropy, while in other planes, the waves will have more distorted shapes. We also demonstrated how the code captures reflections off the material discontinuity boundaries. Lastly, we presented a simulation example where a displacement wave propagates in a layered heterogeneous and fractured medium. There we highlighted the effect of the fracture acting as a barrier for the wave, resulting in the wave being reflected. We have thus shown that the present finite volume method is applicable for solving elastic wave propagation problems in anisotropic, heterogeneous and fractured porous media. This indicates that there is a potential for a unified finite volume method in poromechanical modelling with the inclusion of seismic effects.

Acknowledgements

This project has received funding from the European Research Council (ERC) under the European Union's Horizon 2020 research and innovation program (grant agreement No. 101002507).

Appendix A

For the convergence analysis of the MPSA-Newmark we used the method of manufactured solution. Here are the expressions for the initial displacement, velocity and acceleration, as well as the expression of the source term corresponding to that solution.

Displacement is denoted $u = [u_x, u_y, u_z]^T$. Each component is determined according to:

$$u_i = \sin\left(\frac{5\pi}{2}t\right)xyz(1-x)(1-y)(1-z), \quad i = x, y, z.$$

Velocity is denoted $\dot{u} = [\dot{u}_x, \dot{u}_y, \dot{u}_z]^T$. Each component is determined according to:

$$\dot{u}_i = \frac{5\pi}{2} \cos\left(\frac{5\pi}{2}t\right)xyz(1-x)(1-y)(1-z), \quad i = x, y, z.$$

Acceleration is denoted $\ddot{u} = [\ddot{u}_x, \ddot{u}_y, \ddot{u}_z]^T$. Each component is determined according to:

$$\ddot{u}_i = -\frac{25\pi^2}{4} \sin\left(\frac{5\pi}{2}t\right)xyz(1-x)(1-y)(1-z), \quad i = x, y, z.$$

Source term:

$$q = \sin\left(\frac{5}{2}\pi t\right) [q_x, q_y, q_z]^T,$$

where q_x , q_y and q_z are defined as follows:

$$\begin{aligned} q_x = & -\frac{25\pi^2}{4}xyz(1-x)(1-y)(1-z) - 2.0xyz(1-y) - 2.0xyz(1-z) \\ & + 2.0xy(1-x)(1-y) + 2.0xy(1-y)(1-z) \\ & + 2.0xz(1-x)(1-z) + 2.0xz(1-y)(1-z) \\ & + 2.0yz(1-x)(1-y) + 2.0yz(1-x)(1-z) \\ & + 6.0yz(1-y)(1-z) - 2.0y(1-x)(1-y)(1-z) \\ & - 2.0z(1-x)(1-y)(1-z), \end{aligned}$$

$$\begin{aligned} q_y = & -\frac{25\pi^2}{4}xyz(1-x)(1-y)(1-z) - 2.0xyz(1-x) - 2.0xyz(1-z) \\ & + 2.0xy(1-x)(1-y) + 2.0xy(1-x)(1-z) \\ & + 2.0xz(1-x)(1-y) + 6.0xz(1-x)(1-z) \\ & + 2.0xz(1-y)(1-z) - 2.0x(1-x)(1-y)(1-z) \\ & + 2.0yz(1-x)(1-z) + 2.0yz(1-y)(1-z) \\ & - 2.0z(1-x)(1-y)(1-z), \end{aligned}$$

$$\begin{aligned}
q_z = & -\frac{25\pi^2}{4}xyz(1-x)(1-y)(1-z) - 2.0xyz(1-x) - 2.0xyz(1-y) \\
& + 6.0xy(1-x)(1-y) + 2.0xy(1-x)(1-z) \\
& + 2.0xy(1-y)(1-z) + 2.0xz(1-x)(1-y) \\
& + 2.0xz(1-x)(1-z) - 2.0x(1-x)(1-y)(1-z) \\
& + 2.0yz(1-x)(1-y) + 2.0yz(1-y)(1-z) \\
& - 2.0y(1-x)(1-y)(1-z).
\end{aligned}$$

Appendix B

Here we present how we find the expression for the rotated wave. The procedure is to rotate the orthogonal wave and its coordinates by an angle θ . We start with the expression for the orthogonal wave:

$$u(x, t) = \begin{bmatrix} \sin\left(t - \frac{x}{c_p}\right) \\ 0 \end{bmatrix},$$

We rotate it by applying the two-dimensional rotation matrix as follows:

$$\mathbf{R} u(x, t) = \begin{bmatrix} \cos(\theta) & -\sin(\theta) \\ \sin(\theta) & \cos(\theta) \end{bmatrix} \begin{bmatrix} \sin\left(t - \frac{x}{c_p}\right) \\ 0 \end{bmatrix}.$$

This results in the expression for the wave in terms of the rotated coordinate x' :

$$u(x', t) = \begin{bmatrix} \cos(\theta) \sin\left(t - \frac{x'}{c_p}\right) \\ \sin(\theta) \sin\left(t - \frac{x'}{c_p}\right) \end{bmatrix}.$$

Finally, we also rotate the coordinates:

$$\begin{bmatrix} x' \\ y' \end{bmatrix} = \begin{bmatrix} \cos(\theta) & \sin(\theta) \\ -\sin(\theta) & \cos(\theta) \end{bmatrix} \begin{bmatrix} x \\ y \end{bmatrix} \Rightarrow x' = \cos(\theta)x + \sin(\theta)y,$$

obtaining, by insertion into the rotated solution:

$$u(x, y, t) = \begin{bmatrix} \cos(\theta) \sin\left(t - \frac{\cos(\theta)x + \sin(\theta)y}{c_p}\right) \\ \sin(\theta) \sin\left(t - \frac{\cos(\theta)x + \sin(\theta)y}{c_p}\right) \end{bmatrix}.$$

Then, the expression for the velocity and acceleration is as follows:

$$\dot{u}(x, y, t) = \begin{bmatrix} \cos(\theta) \cos\left(t - \frac{\cos(\theta)x + \sin(\theta)y}{c_p}\right) \\ \sin(\theta) \cos\left(t - \frac{\cos(\theta)x + \sin(\theta)y}{c_p}\right) \end{bmatrix},$$

$$\ddot{u}(x, y, t) = \begin{bmatrix} -\cos(\theta) \sin\left(t - \frac{\cos(\theta)x + \sin(\theta)y}{c_p}\right) \\ -\sin(\theta) \sin\left(t - \frac{\cos(\theta)x + \sin(\theta)y}{c_p}\right) \end{bmatrix}.$$

At initialization we thus have the following expressions for displacement, velocity and acceleration:

$$u(x, y) = \begin{bmatrix} \cos(\theta) \sin\left(-\frac{\cos(\theta)x + \sin(\theta)y}{c_p}\right) \\ \sin(\theta) \sin\left(-\frac{\cos(\theta)x + \sin(\theta)y}{c_p}\right) \end{bmatrix},$$

$$\dot{u}(x, y) = \begin{bmatrix} \cos(\theta) \cos\left(-\frac{\cos(\theta)x + \sin(\theta)y}{c_p}\right) \\ \sin(\theta) \cos\left(-\frac{\cos(\theta)x + \sin(\theta)y}{c_p}\right) \end{bmatrix},$$

$$\ddot{u}(x, y) = \begin{bmatrix} -\cos(\theta) \sin\left(-\frac{\cos(\theta)x + \sin(\theta)y}{c_p}\right) \\ -\sin(\theta) \sin\left(-\frac{\cos(\theta)x + \sin(\theta)y}{c_p}\right) \end{bmatrix}.$$

References

- Berre, I., Boon, W. M., Flemisch, B., Fumagalli, A., Gläser, D., Keilegavlen, E., Scotti, A., Stefansson, I., Tatomir, A., Brenner, K., Burbulla, S., Devloo, P., Duran, O., Favino, M., Hennicker, J., Lee, I. H., Lipnikov, K., Masson, R., Mosthaf, K.,...Zulian, P. (2021). Verification benchmarks for single-phase flow in three-dimensional fractured porous media. *Advances in Water Resources*, 147, 103759. <https://doi.org/10.1016/j.advwatres.2020.103759>
- Cardiff, P., & Demirdžić, I. (2021). Thirty Years of the Finite Volume Method for Solid Mechanics. *Archives of Computational Methods in Engineering*, 28(5), 3721-3780. <https://doi.org/10.1007/s11831-020-09523-0>
- Chopra, A. K. (2012). *Dynamics of Structures*. Pearson Education. <https://books.google.no/books?id=eRcvAAAAQBAJ>
- Clayton, R., & Engquist, B. (1977). Absorbing boundary conditions for acoustic and elastic wave equations. *Bulletin of the Seismological Society of America*, 67(6), 1529-1540. <https://doi.org/10.1785/bssa0670061529>
- Demirdzic, I., Martinovic, D., & Ivankovic, A. (1988). Numerical simulation of thermal deformation in welded workpiece. 31, 209-219.
- Dormy, E., & Tarantola, A. (1995). Numerical simulation of elastic wave propagation using a finite volume method. *Journal of Geophysical Research: Solid Earth*, 100(B2), 2123-2133. <https://doi.org/10.1029/94JB02648>
- Dumbser, M., Käser, M., & De La Puente, J. (2007). Arbitrary high-order finite volume schemes for seismic wave propagation on unstructured meshes in 2D and 3D. *Geophysical Journal International*, 171(2), 665-694. <https://doi.org/10.1111/j.1365-246X.2007.03421.x>
- Ferguson, J. C., Panerai, F., Borner, A., & Mansour, N. N. (2018). PuMA: the Porous Microstructure Analysis software. *SoftwareX*, 7, 81-87. <https://doi.org/10.1016/j.softx.2018.03.001>
- Higdon, R. L. (1991). Absorbing boundary conditions for elastic waves. *GEOPHYSICS*, 56(2), 231-241. <https://doi.org/10.1190/1.1443035>
- Igel, H. (2016). *Computational Seismology: A Practical Introduction*. Oxford University Press.
- Jacobsen, I. K., Berre, I., Nordbotten, J. M., & Stefansson, I. (2024). Source Code: A Finite Volume Method for Elastic Waves in Heterogeneous, Anisotropic and Fractured Media. <https://doi.org/10.5281/zenodo.13861514>
- Keilegavlen, E., Berge, R., Fumagalli, A., Starnoni, M., Stefansson, I., Varela, J., & Berre, I. (2021). PorePy: an open-source software for simulation of multiphysics processes in fractured porous media. *Computational Geosciences*, 25(1), 243-265. <https://doi.org/10.1007/s10596-020-10002-5>
- Keilegavlen, E., & Nordbotten, J. M. (2017). Finite volume methods for elasticity with weak symmetry. *International Journal for Numerical Methods in Engineering*, 112(8), 939-962. <https://doi.org/10.1002/nme.5538>
- Kim, J., Tchelep, H. A., & Juanes, R. (2011). Stability and convergence of sequential methods for coupled flow and geomechanics: Fixed-stress and fixed-strain splits. *Computer Methods in Applied Mechanics and Engineering*, 200(13), 1591-1606. <https://doi.org/10.1016/j.cma.2010.12.022>
- Knabner, P., & Angermann, L. (2003). *Numerical Methods for Elliptic and Parabolic Partial Differential Equations*. Springer. <https://doi.org/10.1007/b97419>
- Lemoine, G. I., & Ou, M. Y. (2014). Finite Volume Modeling of Poroelastic-Fluid Wave Propagation with Mapped Grids. *SIAM Journal on Scientific Computing*, 36(3), B396-B426. <https://doi.org/10.1137/130920824>

- Lemoine, G. I., Ou, M. Y., & LeVeque, R. J. (2013). High-Resolution Finite Volume Modeling of Wave Propagation in Orthotropic Poroelastic Media. *SIAM Journal on Scientific Computing*, 35(1), B176-B206. <https://doi.org/10.1137/120878720>
- Lie, K. A. (2019). *An Introduction to Reservoir Simulation Using MATLAB/GNU Octave: User Guide for the MATLAB Reservoir Simulation Toolbox (MRST)*. Cambridge University Press. <https://doi.org/10.1017/9781108591416>
- Newmark, N. M. (1959). A Method of Computation for Structural Dynamics. *Journal of the Engineering Mechanics Division*, 85(3), 67-94. <https://doi.org/10.1061/JMCEA3.0000098>
- Nordbotten, J. M. (2014). Cell-centered finite volume discretizations for deformable porous media. *International Journal for Numerical Methods in Engineering*, 100(6), 399-418. <https://doi.org/10.1002/nme.4734>
- Nordbotten, J. M. (2016). Stable Cell-Centered Finite Volume Discretization for Biot Equations. *SIAM Journal on Numerical Analysis*, 54(2), 942-968. <https://doi.org/10.1137/15m1014280>
- Nordbotten, J. M., & Keilegavlen, E. (2021). An Introduction to Multi-Point Flux (MPFA) and Stress (MPSA) Finite Volume Methods for Thermo-Poroelasticity. In D. A. Di Pietro, L. Formaggia, & R. Masson (Eds.), *Polyhedral Methods in Geosciences* (pp. 119-158). Springer International Publishing. https://doi.org/10.1007/978-3-030-69363-3_4
- Novikov, A., Voskov, D., Khait, M., Hajibeygi, H., & Jansen, J. D. (2022). A scalable collocated finite volume scheme for simulation of induced fault slip. *Journal of Computational Physics*, 469, 111598. <https://doi.org/10.1016/j.jcp.2022.111598>
- Payton, R. (2012). *Elastic wave propagation in transversely isotropic media* (Vol. 4). Springer Science & Business Media. <https://doi.org/10.1007/978-94-009-6866-0>
- Seriani, G., & Oliveira, S. P. (2020). Numerical modeling of mechanical wave propagation. *La Rivista del Nuovo Cimento*, 43(9), 459-514. <https://doi.org/10.1007/s40766-020-00009-0>
- Subbaraj, K., & Dokainish, M. A. (1989). A survey of direct time-integration methods in computational structural dynamics—II. Implicit methods. *Computers & Structures*, 32(6), 1387-1401. [https://doi.org/10.1016/0045-7949\(89\)90315-5](https://doi.org/10.1016/0045-7949(89)90315-5)
- Tadi, M. (2004). Finite Volume Method for 2D Elastic Wave Propagation. *Bulletin of the Seismological Society of America*, 94(4), 1500-1509. <https://doi.org/10.1785/012003138>
- Terekhov, K. M. (2020). Cell-centered finite-volume method for heterogeneous anisotropic poromechanics problem. *Journal of Computational and Applied Mathematics*, 365, 112357. <https://doi.org/10.1016/j.cam.2019.112357>
- Terekhov, K. M., & Tchelepi, H. A. (2020). Cell-centered finite-volume method for elastic deformation of heterogeneous media with full-tensor properties. *Journal of Computational and Applied Mathematics*, 364, 112331. <https://doi.org/10.1016/j.cam.2019.06.047>
- Terekhov, K. M., & Vassilevski, Y. V. (2022). Finite volume method for coupled subsurface flow problems, II: Poroelasticity. *Journal of Computational Physics*, 462, 111225. <https://doi.org/10.1016/j.jcp.2022.111225>
- Tsogka, C. (1999). *Modélisation mathématique et numérique de la propagation des ondes élastiques tridimensionnelles dans des milieux fissurés*
- Tuković, Ž., Ivanković, A., & Karač, A. (2013). Finite-volume stress analysis in multi-material linear elastic body. *International Journal for Numerical Methods in Engineering*, 93(4), 400-419. <https://doi.org/10.1002/nme.4390>
- Verwer, J. G., & Sanz-Serna, J. M. (1984). *Convergence of method of lines approximations to partial differential equations*. CWI. Department of Numerical Mathematics [NM].

- Virieux, J., Calandra, H., & Plessix, R.-É. (2011). A review of the spectral, pseudo-spectral, finite-difference and finite-element modelling techniques for geophysical imaging. *Geophysical Prospecting*, 59(5), 794-813. <https://doi.org/10.1111/j.1365-2478.2011.00967.x>
- Zhang, W., Zhuang, Y., & Chung, E. T. (2016). A new spectral finite volume method for elastic wave modelling on unstructured meshes. *Geophysical Journal International*, 206(1), 292-307. <https://doi.org/10.1093/gji/ggw148>
- Zhang, W., Zhuang, Y., & Zhang, L. (2017). A new high-order finite volume method for 3D elastic wave simulation on unstructured meshes. *Journal of Computational Physics*, 340, 534-555. <https://doi.org/10.1016/j.jcp.2017.03.050>
- Aavatsmark, I. (2002). An Introduction to Multipoint Flux Approximations for Quadrilateral Grids. *Computational Geosciences*, 6(3), 405-432. <https://doi.org/10.1023/A:1021291114475>